






Fabrication of 100-nm-period domain structure in lithium niobate on insulator

JIANAN MA,¹ XIAOYAN CHENG,¹ NINGCHONG ZHENG,¹
PENGCHENG CHEN,¹ XIAOYI XU,¹ TIANXIN WANG,¹
DUNZHAO WEI,²  YUEFENG NIE,¹ SHINING ZHU,¹ MIN XIAO,^{1,3} 
AND YONG ZHANG^{1,*} 

¹National Laboratory of Solid State Microstructures, College of Engineering and Applied Sciences, and Collaborative Innovation Center of Advanced Microstructures, Nanjing University, Nanjing 210093, China

²State Key Laboratory of Optoelectronic Materials and Technologies, School of Physics, Sun Yat-Sen University, Guangzhou 510275, China

³Department of Physics, University of Arkansas, Fayetteville, Arkansas 72701, USA

*zhangyong@nju.edu.cn

Abstract: Lithium niobate on insulator (LNOI) is a powerful platform for integrated photonic circuits. Recently, advanced applications in nonlinear and quantum optics require to controllably fabricate nano-resolution domain structures in LNOI. Here, we report on the fabrication of stable domain structures with sub-100 nm feature size through piezoelectric force microscopy (PFM) tip poling in a z-cut LNOI. In experiment, the domain dot with an initial diameter of 80 nm and the domain line with an initial width of 50 nm can survive after a storage of more than 3 months. Particularly, we demonstrate the successful fabrication of 1D stable domain array with a period down to 100 nm and a duty cycle of ~50%. Our method paves the way to precisely manipulate frequency conversion and quantum entanglement on an LNOI chip.

© 2023 Optica Publishing Group under the terms of the [Optica Open Access Publishing Agreement](#)

1. Introduction

Lithium niobate on insulator (LNOI) is one promising and versatile material in the field of integrated photonics due to its superior material properties and high confinement of optical mode [1–3]. High-quality LNOI photonic elements such as ultra-low-loss waveguides [4,5], high Q-factor microresonators [6] and photonic crystals [7] have been experimentally demonstrated, which considerably boost the developments of on-chip wavelength converters [8–10], electro-optic modulators [11,12], and optical frequency combs [13]. Interestingly, combined with periodically poled domain structures, LNOI is capable of enhancing the conversion efficiency of nonlinear optical processes through quasi-phase-matching (QPM) [14] mechanism.

Among the techniques to fabricate domain structures [15–20], piezoelectric force microscopy (PFM) tip poling is particularly useful for nanoscale domain engineering [21–23]. The nanoscale tip can produce an ultrahigh electric field of $\sim 10^8$ V/m by applying a bias voltage of tens of volts [24,25]. It has been utilized to realize LNOI periodic domain structure with its period down to 200 nm [26,27]. However, many practical applications require much smaller domain structures. For example, nonlinear optical processes under counter-propagating configuration, such as mirrorless optical parametric oscillators (MOPO) [28] and backward second harmonic generation (SHG) [29], feature output signals of narrow linewidths. To compensate the large wave-vector mismatch in these cases [30], it is necessary to further reduce the domain structure period. For example, it is critical to fabricate LNOI domain structure with a period down to 100 nm to satisfy the QPM condition for the backward outputs of narrow-band signal and idler quantum lights through spontaneous parametric down conversion (SPDC) process.

In this letter, we demonstrate the fabrication of sub-100-nm domain structures in z-cut LNOI thin films through PFM tip poling. In experiment, we measure the size dependences

of dotted domains and domain lines under different experimental conditions. After analyzing the nanodomain stability, we optimize the poling parameters. For a stable domain structure (that survives after a storage of 3 months) in our experiment, the minimal domain linewidth is ~ 50 nm and the minimal structure period with a duty cycle of $\sim 50\%$ is ~ 100 nm. Such nanoscale poling technology facilitates the precise fabrication of nanoscale domain structures in LNOI for applications in nanoelectronics, integrated optics, and nonlinear frequency conversion.

2. Methods

We use a +z-cut ion-sliced LNOI wafer (Jinan Jingzheng Electronics Co., Ltd. China). As shown in Fig. 1, the sample consists of a 400-nm-thick LN thin film on a Cr/Au/Cr (30 nm / 100 nm / 10 nm) conductive layer bonded on a SiO₂ buffer layer (2 μ m) and a LN substrate (500 μ m). The coercive electric field of the used sample is measured through switching spectroscopy PFM (SS-PFM) measurement. In experiment, the conductive layer is grounded by conductive silver glue. The positive bias voltage is applied to the sample through a conductive PFM tip, which is a Pt/Ir-coated silicon probe with a radius of ~ 33 nm (Arrow-EFM, Nanoworld). The effective electric field is analyzed by using the theory in [24,25]. The experiments are performed through a dual AC resonance tracking PFM (featuring 0.8~1.5 V AC voltage and ~ 300 kHz resonant frequency) using a scanning probe microscope (MFP 3D, Asylum Research, USA). The temperature is $\sim 25^\circ\text{C}$ and the relative humidity is $\sim 35\%$. All experimental data are analyzed and recorded using Igor software.

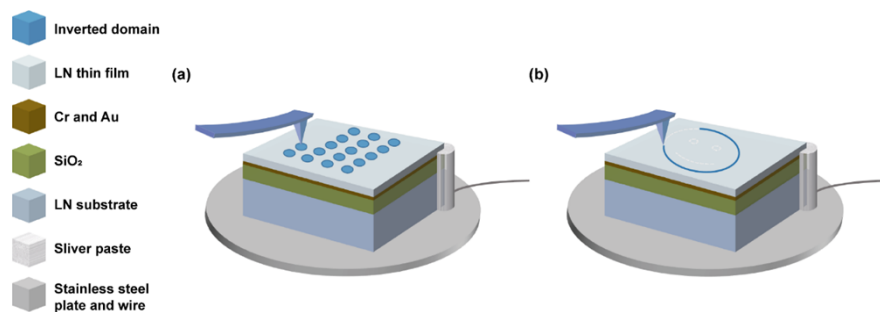


Fig. 1. The schematic diagrams of PFM tip poling of (a) nanodomain dots and (b) nanodomain lines.

3. Experimental results and discussion

We start with the poling of nanodomain dots by applying DC voltage pulses with different amplitudes U_{DC} and durations τ to the conductive tip. The experiment is conducted in a static contact mode (Fig. 1(a)). The interval between the domain dots is set to 0.5 μ m. The pulse amplitude ranges from 5 V to 50 V and the pulse duration ranges from 1 μ s to 20s.

Figure 2(a) is the PFM phase image of the generated domain dots. The inverted domains present a circular symmetry, and the measured domain diameters range from tens of nanometers to 300 nm. When applying a voltage of 15 V with a duration of 10 s, we achieve the minimal domain diameter of ~ 25 nm. No domain dots are observed when pulse amplitude is below 15 V. It can be clearly observed that the threshold voltage of domain inversion decreases as increasing the pulse duration τ . As shown in Fig. 2(c), the domain diameter grows up linearly with U_{DC} , which is consistent with the previous studies [23,31]. Figure 2(d) shows the dependence of the domain diameter on the pulse duration τ . When $\tau > 0.01$ s, one can read a clear logarithmical relationship. In contrast, when $\tau < 0.01$ s, the domain diameters are almost constant as tuning the pulse duration. This can be explained by the theory of starter domain [32]. During this stage, the

longitudinal growth of domain dominates while its lateral extension can be neglected. According to Merz's law [33], the sizes of the starter domains under different experimental conditions can be obtained by fitting the cutoff points of the curves in Fig. 2(d). When applying an electric field of 25 V, 30 V, 35 V, 40 V, 45 V, and 50 V, the sizes of the starter domains are 34 nm, 76 nm, 114 nm, 145 nm, 177 nm, and 206 nm, respectively.

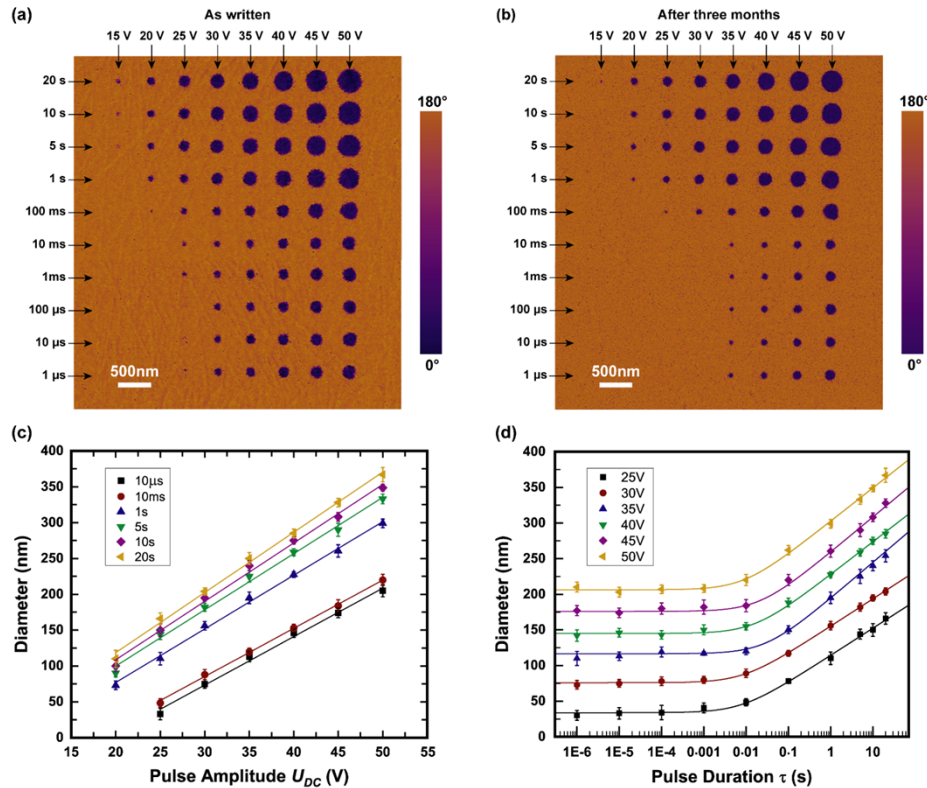


Fig. 2. The characteristics of nanodomain dots. (a) The PFM phase images of the domain dots under various DC voltage pulses. (b) shows the results after a three-month storage. (c) The domain dot diameter as a function of the pulse amplitude U_{DC} . (d) The dependence of domain dot diameters on the pulse duration τ is fitted by using $y = a \ln(bx + c)$. The errors could result from the condition of PFM tips, the non-uniform LNOI sample, and non-ideal electrode quality.

Figure 2(b) presents the stability test results of the domain dots in Fig. 2(a) after a storage of 3 months. The domain dots with initial diameters above 80 nm shrink but still exist in our experiment. Smaller domain dots are instable and generally disappear within several days. The domain dots fabricated by using τ or U_{DC} below the threshold values present poor stability. This can be attributed to inadequate charge injection and thus incomplete screening of depolarization field [34].

When writing the nanodomain lines, we use a DC-biased tip and precisely design its movement path using MicroAngelo software as shown in Fig. 1(b). Thus, each domain line can be written under nearly the same scanning velocity and bias voltage in one step. In experiment, we compare domain lines by tuning the bias voltage from 20 to 40 V and the scanning velocity from 0.1 to 20 $\mu\text{m/s}$. Figure 3(a) presents the typical PFM phase images of domain lines by using a fixed scanning velocity of 0.2 $\mu\text{m/s}$ but various poling voltages (top). Figure 3(b) compares the domain lines written at a fixed bias voltage of 20 V while changing the scanning velocity

(top). Figures 3(c) and 3(d) summarize the dependences of the domain linewidth on the bias voltage and scanning velocity, which fit well with linear and negatively logarithmic functions, respectively. In our experiment, the minimal realizable domain linewidth is 25 nm (Fig. 3(b)), which, however, survives only for several days. As shown in Figs. 3(a) and 3(b), the domain lines with an initial linewidth above 50 nm can survive after a 3-month storage. In comparison, the finer ones completely or partially disappear. The threshold size of a stable domain line (50 nm) is much smaller than that of a stable domain dot (80 nm) in our experiment. This can be attributed to the fact that the ratio of domain wall in a domain line is much smaller than that in a domain dot. This helps reduce the surface energy of the domain wall and then the total free energy of the domain structure [35].

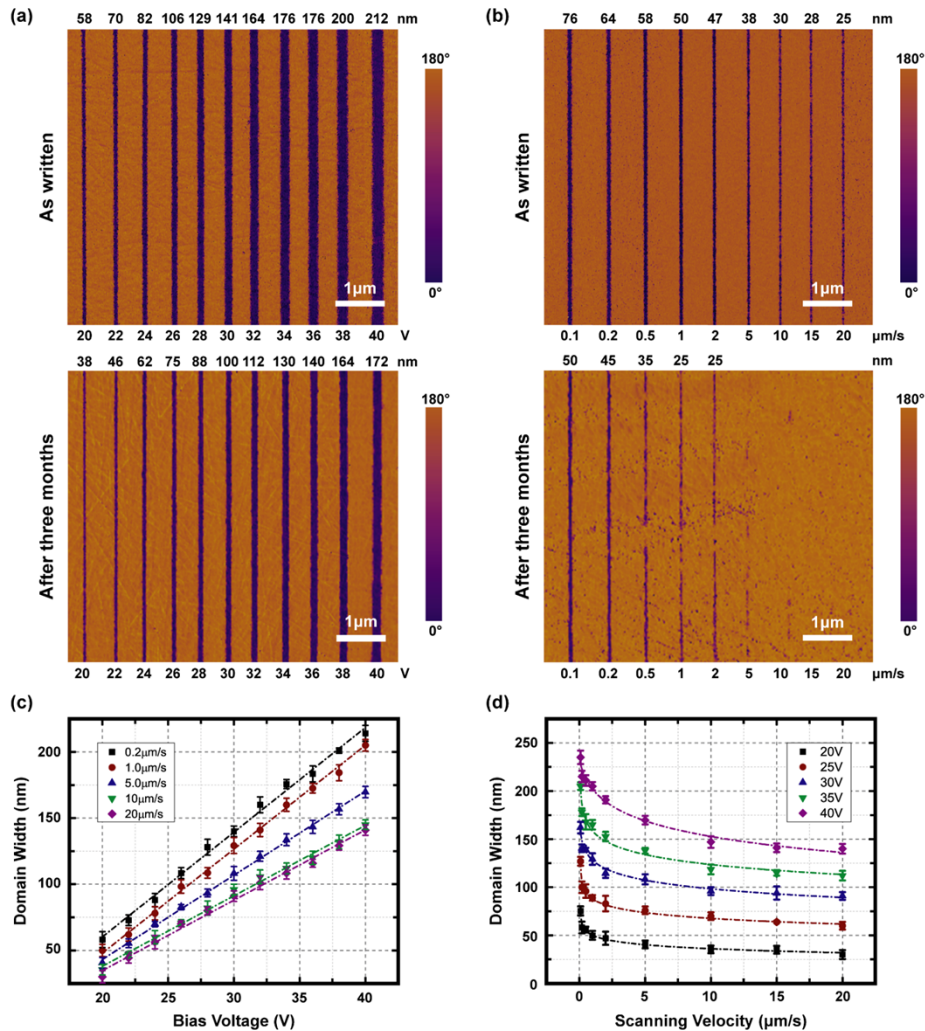


Fig. 3. The characteristics of nanodomain lines. (a) The phase image of the domain lines written by applying various bias voltages (top). The results after a three-month storage are shown in the bottom. The scanning velocity is set to 0.2 μm/s. (b) The phase image of the domain lines written at different scanning speed (top). The bottom image shows the results after a three-month storage. The bias voltage is kept at 20 V. (c) and (d) show the dependences of the domain linewidth on the bias voltage and scanning velocity, respectively. The experimental data in (d) is fitted by using $y = a - bln(x + c)$.

We have also fabricated periodic nanodomain arrays in LNOI, which are particularly useful in the generation of narrowband signal and idler lights for quantum applications. Figures 4(a)-(c) show the phase images of three stable examples. The domain array in Fig. 4(a) has a period of $164 \text{ nm} \pm 6 \text{ nm}$ and a linewidth of $92 \text{ nm} \pm 8 \text{ nm}$, which is fabricated at 25 V voltage and $2.5 \mu\text{m/s}$ scanning speed. When using 22 V voltage and $1 \mu\text{m/s}$ scanning speed, the array in Fig. 4(b) has a period of $144 \text{ nm} \pm 3 \text{ nm}$ and a linewidth of $75 \pm 4 \text{ nm}$. Figure 4(c) shows the minimal period under our current experimental system. The period is $102 \pm 4 \text{ nm}$ and the linewidth is $53 \pm 5 \text{ nm}$. The used bias voltage is 20 V and the scanning speed is $2 \mu\text{m/s}$. After a five-months storage, we have re-measured these domain arrays as shown in Figs. 4(d)-(f), one can still observe clear periodic nanodomain structures. Here, alternative arrangement of positive and negative domains could reduce the local free energy, which helps increase the domain stability. According to previous reports [36], high humidity could have severe impact on domain stability. In our experiment, the samples were hermetically sealed for preservation at a temperature of $\sim 25^\circ\text{C}$ and a relative humidity of $\sim 35\%$. To further improve the stability of nanodomain structures in practical applications, one may deposit a SiO_2 layer on the LN thin films as the upper-cladding [37]. In this way, the environmental conditions that may have negative effects on domain stability, including electric charges and humidity, can be well screened.

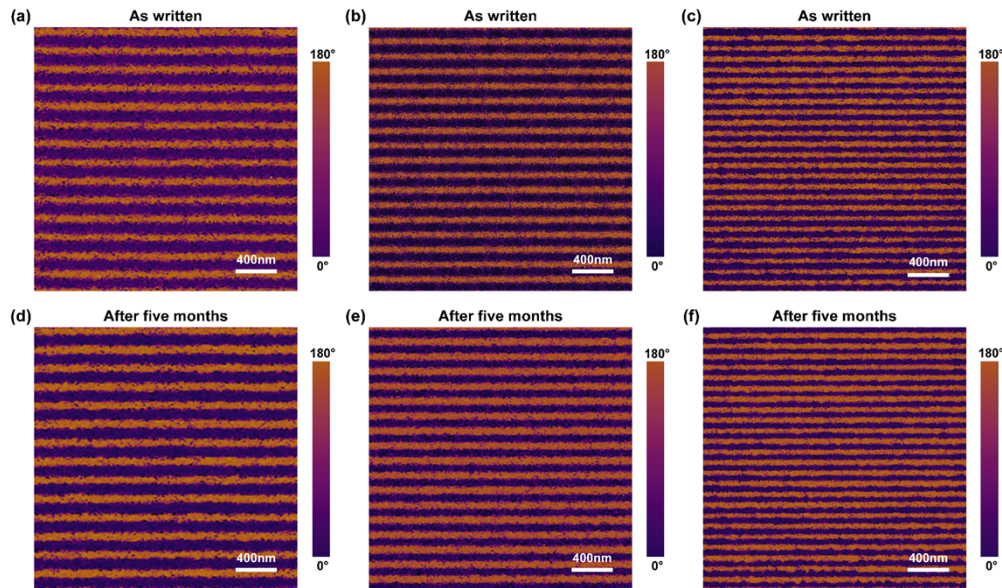


Fig. 4. The characteristics of nanodomain arrays. (a)-(c) are nanodomain arrays with the periods of 164 nm, 144 nm, and 102 nm, respectively. (d)-(f) show the domain patterns after a five-months storage. The samples were hermetically sealed for preservation at a temperature of $\sim 25^\circ\text{C}$ and a relative humidity of $\sim 35\%$. Clearly, these nanodomain arrays have successfully survived.

In addition, we have performed the thermal stability test. The sample is heated from room temperature to 100°C in air at a rate of $5^\circ\text{C}/\text{min}$. Then, it is maintained at 100°C for 40 minutes before being cooled down naturally to room temperature in air. As shown in Fig. 5, the domain dots generally shrink and the small ones completely disappear. In comparison, the periodic domain lines present much better stability. The periodicity is well preserved and the domain linewidth is slightly reduced. The improved stability of the domain lines can be attributed to the reduced surface energy and depolarizing energy [35,38].

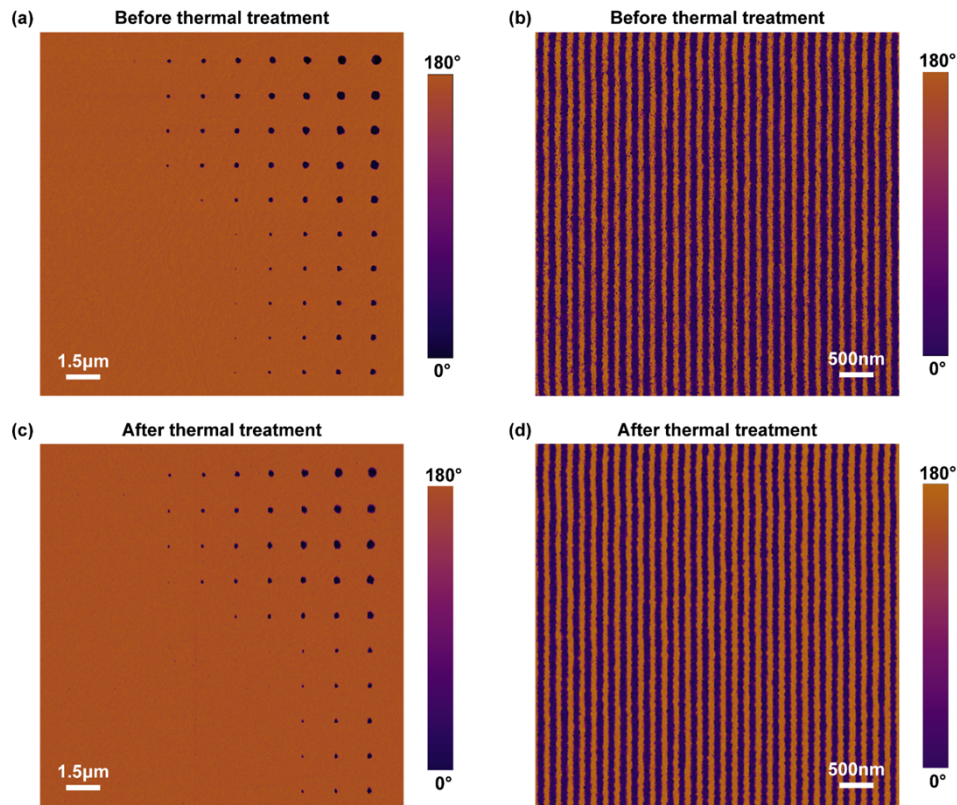


Fig. 5. The thermal stability test. (a) and (b) show the original domain dots and periodic domains. (c) and (d) present the results after thermal treatment.

4. Conclusion

In summary, we have demonstrated the fabrications of LNOI nanodomain dots, lines, and arrays with sub-100 nm feature size and good stability. PFM tip poling technique has been proven capable of maskless printing LNOI domains with ultrahigh resolution. Although it is difficult to fabricate large-area domain structures, PFM tip poling is useful in the fabrication of periodically poled LNOI micro-resonators for on-chip applications. In this work, the poling parameters including bias voltage and scanning speed are carefully optimized to approach the experimental limit of our system (~ 50 nm). To further reduce the nanodomain size while keeping it stable, one may optimize the tip profile to better control the electric field.

Funding. National Key Research and Development Program of China (2022YFA1205100, 2021YFA1400400, 2022YFA1402502); National Natural Science Foundation of China (91950206, 92163216); China Postdoctoral Science Foundation (2023M731587, 2023T160303); Yuxiu Young Scholars Program of Nanjing University; Guangdong Natural Science Funds for Distinguished Young Scholars (2022B1515020067); Guangzhou Science and Technology Plan Foundation and Application Foundation Research Project (202201011270).

Disclosures. The authors declare that there are no conflicts of interest related to this article.

Data availability. The data that support the findings of this study are available from the corresponding author upon reasonable request.

References

1. A. Boes, B. Corcoran, and L. Chang, *et al.*, "Status and potential of lithium niobate on insulator (LNOI) for photonic integrated circuits," *Laser Photonics Rev.* **12**(4), 1700256 (2018).

2. M. G. Vazimali and S. Fathpour, "Applications of thin-film lithium niobate in nonlinear integrated photonics," *Adv. Photonics* **4**(03), 034001 (2022).
3. H. Zhu, Q. Li, and H. Han, *et al.*, "Hybrid mono-crystalline silicon and lithium niobate thin films [Invited]," *Chin. Opt. Lett.* **19**(6), 060017 (2021).
4. M. Zhang, C. Wang, and R. Cheng, *et al.*, "Monolithic ultra-high-Q lithium niobate microring resonator," *Optica* **4**(12), 1536–1537 (2017).
5. R. Wu, M. Wang, and J. Xu, *et al.*, "Long low-loss-lithium niobate on insulator waveguides with sub-nanometer surface roughness," *Nanomaterials* **8**(11), 910 (2018).
6. R. Gao, H. Zhang, and F. Bo, *et al.*, "Broadband highly efficient nonlinear optical processes in on-chip integrated lithium niobate microdisk resonators of Q-factor above 10^8 ," *New J. Phys.* **23**(12), 123027 (2021).
7. M. Li, J. Ling, and Y. He, *et al.*, "Lithium niobate photonic-crystal electro-optic modulator," *Nat. Commun.* **11**(1), 4123 (2020).
8. S. Yuan, Y. Wu, and Z. Dang, *et al.*, "Strongly enhanced second harmonic generation in a thin film lithium niobate heterostructure cavity," *Phys. Rev. Lett.* **127**(15), 153901 (2021).
9. Y. Zheng and X. Chen, "Nonlinear wave mixing in lithium niobate thin film," *Adv. Phys.: X* **6**(1), 1889402 (2021).
10. M. Jankowski, C. Langrock, and B. Desiatov, *et al.*, "Ultrabroadband nonlinear optics in nanophotonic periodically poled lithium niobate waveguides," *Optica* **7**(1), 40–46 (2020).
11. C. Wang, M. Zhang, and X. Chen, *et al.*, "Integrated lithium niobate electro-optic modulators operating at CMOS-compatible voltages," *Nature* **562**(7725), 101–104 (2018).
12. M. He, M. Xu, and Y. Ren, *et al.*, "High-performance hybrid silicon and lithium niobate Mach–Zehnder modulators for 100 Gbit s^{-1} and beyond," *Nat. Photonics* **13**(5), 359–364 (2019).
13. Y. Hu, M. Yu, and B. Buscaino, *et al.*, "High-efficiency and broadband on-chip electro-optic frequency comb generators," *Nat. Photonics* **16**(10), 679–685 (2022).
14. J. A. Armstrong, N. Bloembergen, and J. Ducuing, *et al.*, "Interactions between light waves in a nonlinear dielectric," *Phys. Rev.* **127**(6), 1918–1939 (1962).
15. J. Zhao, M. Ruesing, and M. Roeper, *et al.*, "Poling thin-film x-cut lithium niobate for quasi-phase matching with sub-micrometer periodicity," *J. Appl. Phys.* **127**(19), 193104 (2020).
16. A. Boes, V. Sivan, and G. Ren, *et al.*, "Precise, reproducible nano-domain engineering in lithium niobate crystals," *Appl. Phys. Lett.* **107**(2), 022901 (2015).
17. D. S. Chezganov, E. O. Vlasov, and E. A. Pashnina, *et al.*, "Domain patterning of non-polar cut lithium niobate by focused ion beam," *Ferroelectrics* **559**(1), 66–76 (2020).
18. M. Yamada and K. Kishima, "Fabrication of periodically reversed domain structure for SHG in LiNbO₃ by direct electron beam lithography at room temperature," *Electron. Lett.* **27**(10), 828–829 (1991).
19. H. Steigerwald, Y. J. Ying, and R. W. Eason, *et al.*, "Direct writing of ferroelectric domains on the x- and y-faces of lithium niobate using a continuous wave ultraviolet laser," *Appl. Phys. Lett.* **98**(6), 062902 (2011).
20. X. Xu, T. Wang, and P. Chen, *et al.*, "Femtosecond laser writing of lithium niobate ferroelectric nanodomains," *Nature* **609**(7927), 496–501 (2022).
21. Y. Qian, Z. Zhang, and Y. Liu, *et al.*, "Graphical direct writing of macroscale domain structures with nanoscale spatial resolution in nonpolar-cut lithium niobate on insulators," *Phys. Rev. Appl.* **17**(5), 054049 (2022).
22. W. Ge, H. Zeng, and Y. Shuai, *et al.*, "Nano-domain nucleation in front of moving domain wall during tip-induced polarization reversal in ion-sliced LiNbO₃ thin films," *Mater. Res. Express* **6**(3), 035033 (2018).
23. B. N. Slautin, A. P. Turygin, and E. D. Greshnyakov, *et al.*, "Domain structure formation by local switching in the ion sliced lithium niobate thin films," *Appl. Phys. Lett.* **116**(15), 152904 (2020).
24. G. Rosenman, P. Urenski, and A. Agronin, *et al.*, "Submicron ferroelectric domain structures tailored by high-voltage scanning probe microscopy," *Appl. Phys. Lett.* **82**(1), 103–105 (2003).
25. E. J. Mele, "Screening of a point charge by an anisotropic medium: anamorphoses in the method of images," *Am. J. Phys.* **69**(5), 557–562 (2001).
26. Z. Hao, L. Zhang, and W. Mao, *et al.*, "Second-harmonic generation using d33 in periodically poled lithium niobate microdisk resonators," *Photonics Res.* **8**(3), 311–317 (2020).
27. B. N. Slautin, H. Zhu, and V. Y. Shur, "Submicron periodical poling in Z-cut lithium niobate thin films," *Ferroelectrics* **576**(1), 119–128 (2021).
28. C. Canalias and V. Pasiskevicius, "Mirrorless optical parametric oscillator," *Nat. Photonics* **1**(8), 459–462 (2007).
29. J. U. Kang, Y. J. Ding, and W. K. Burns, *et al.*, "Backward second-harmonic generation in periodically poled bulk LiNbO₃," *Opt. Lett.* **22**(12), 862–864 (1997).
30. V. Y. Shur, A. R. Akhmatkhanov, and I. S. Baturin, "Micro- and nano-domain engineering in lithium niobate," *Appl. Phys. Rev.* **2**(4), 040604 (2015).
31. R. V. Gainutdinov, T. R. Volk, and H. H. Zhang, "Domain formation and polarization reversal under atomic force microscopy-tip voltages in ion-sliced LiNbO₃ films on SiO₂/LiNbO₃ substrates," *Appl. Phys. Lett.* **107**(16), 162903 (2015).
32. M. Lilienblum and E. Soergel, "Determination of the effective coercive field of ferroelectrics by piezoresponse force microscopy," *J. Appl. Phys.* **110**(5), 052012 (2011).
33. W. J. Merz, "Domain formation and domain wall motions in ferroelectric BaTiO₃ single crystals," *Phys. Rev.* **95**(3), 690–698 (1954).

34. V. Y. Shur, "Kinetics of ferroelectric domains: Application of general approach to LiNbO₃ and LiTaO₃," *J. Mater. Sci.* **41**(1), 199–210 (2006).
35. M. Molotskii, A. Agronin, and P. Urenski, *et al.*, "Ferroelectric domain breakdown," *Phys. Rev. Lett.* **90**(10), 107601 (2003).
36. X. Sun, Y. J. Su, and X. Li, *et al.*, "Stability of nano-scale ferroelectric domains in a LiNbO₃ single crystal: The role of surface energy and polar molecule adsorption," *J. Appl. Phys.* **111**(9), 094110 (2012).
37. A. Shams-Ansari, G. Huang, and L. He, *et al.*, "Reduced material loss in thin-film lithium niobate waveguides," *APL Photonics* **7**(8), 081301 (2022).
38. T. R. Volk, L. V. Simagina, and R. V. Gainutdinov, *et al.*, "Ferroelectric microdomains and microdomain arrays recorded in strontium–barium niobate crystals in the field of atomic force microscope," *J. Appl. Phys.* **108**(4), 042010 (2010).